TRENDS IN SCIENCES 2026; 23(1): 11331
https://doi.org/10.48048/tis.2026.11331 RESEARCH ARTICLE

Quinazolinone Derivatives as Targeting *pf*DHFR and *pf*DHODH Inhibitor: *In Silico* Studies Using Molecular Docking, Molecular Dynamics Simulations, MM-PBSA, and ADMET Analysis

Tendy Oktriawan[1], Bina Agustin Aulia[1], Timur Setyawan[1], Tri Joko Raharjo[1], Winarto Haryadi[1], Laurent Commeiras[2] and Muhammad Idham Darussalam Mardjan[1,*]

[1]*Department of Chemistry, Faculty of Mathematics and Natural Sciences, Universitas Gadjah Mada, Yogyakarta 55281, Indonesia*
[2]*Aix Marseille University, CNRS, Centrale Med, Marseille 13397, France*

([*]Corresponding author's e-mail: idham.darussalam@ugm.ac.id)

Received: 20 July 2025, Revised: 26 August 2025, Accepted: 10 September 2025, Published: 15 October 2025

Abstract

Malaria remains a significant global health concern, with rising resistance to current antimalarial drugs. *pf*DHFR (*Plasmodium falciparum* Dihydrofolate Reductase) and *pf*DHODH (*Plasmodium falciparum* Dihydroorotate Dehydrogenase) are critical enzymes for parasite survival and have emerged as promising targets for drug development. Quinazolinones have shown potential as antimalarial agents due to their diverse pharmacological activities. This study aims to evaluate quinazolinones as potential inhibitors of *pf*DHFR and *pf*DHODH using molecular docking, molecular dynamics simulations, and ADMET (Absorption, Distribution, Metabolism, Excretion and Toxicity) profiling to identify optimal candidates with improved efficacy and pharmacokinetics. Thirty quinazolinone derivatives were subjected to molecular docking against *pf*DHFR and *pf*DHODH to assess binding affinity and interaction modes. Promising compounds were further analyzed through molecular dynamics simulations to evaluate complex stability. Additionally, ADMET profiling was conducted to predict pharmacokinetic properties and toxicity. Molecular docking identified compounds **3**, **5**, and **12** as promising *pf*DHFR inhibitors, with compound **3** exhibiting the most favorable binding energy. For *pf*DHODH, compounds **2**, **11**, and **20** showed strong interactions. Molecular dynamics simulations confirmed the stability of these complexes, with compounds **3** and **5** being stable against *pf*DHFR and compounds **20** and **11** against *pf*DHODH. ADMET analysis revealed favorable drug-like properties for these compounds, although some toxicity concerns were noted. This study demonstrates the potential of quinazolinone derivatives as next-generation antimalarial agents targeting *pf*DHFR and *pf*DHODH. Compounds **3**, **5**, **11**, and 1**2** are identified as promising candidates due to their strong binding affinities and stable pharmacokinetic profiles. Further optimization and experimental validation are necessary to develop these compounds into effective therapeutic agents against malaria.

Keywords: Antimalarial, *pf*DHFR, *pf*DHODH, Quinazolinone, Molecular docking, Molecular dynamics, MM-PBSA, RAM, ADMET

Introduction

Malaria continues to be a pressing global health concern, with an estimated 249 million cases and more than 608,000 fatalities reported in 2022 [1,2]. The disease disproportionately affects sub-Saharan Africa, which accounts for 95% of malaria-related deaths, particularly impacting vulnerable populations such as young children and pregnant women [3]. Among the 6 *Plasmodium* species infecting humans [4,5], *Plasmodium falciparum* is the most severe [6], causing the majority of critical cases due to its rapid proliferation in red blood cells and its potential to trigger

complications like cerebral malaria and organ dysfunction [7].

Efforts to combat malaria face significant obstacles due to the rise of drug-resistant strains of *Plasmodium falciparum*. Resistance has emerged against commonly used antimalarial drugs [8], including chloroquine [9], SP (Sulfadoxine-Pyrimethamine) [10], and even ACTs (artemisinin-based combination therapies) [11], which are widely regarded as the most effective current treatments. This resistance is primarily driven by genetic mutations in key parasite enzymes, including *pf*DHFR and *pf*DHODH, which are critical for parasite survival [12]. *pf*DHODH is essential for pyrimidine biosynthesis, a crucial pathway for the production of DNA and RNA, as the parasite is unable to utilize a pyrimidine salvage mechanism. [13]. Inhibitory compounds targeting the *pf*DHODH enzyme hold potential as antimalarial drugs because they disrupt a vital metabolic pathway essential for the parasite's survival, by disrupting parasite replication by selectively interfering with this pathway [14]. Similarly, *pf*DHFR is a key enzyme involved in folate metabolism required for DNA synthesis [15]. While antifolate drugs like pyrimethamine have been effective in targeting *pf*DHFR, resistance mutations necessitate the development of novel inhibitors that can overcome these mutations while maintaining potency [16].

Quinazolinones have emerged as promising candidates for addressing drug resistance in malaria treatment nowadays. These heterocyclic compounds exhibit diverse pharmacological activities, including potent antimalarial effects [17,18]. Their structural adaptability allows for chemical modifications that enhance their activity against resistant strains of *Plasmodium falciparum*. Their structural flexibility allows for chemical modifications that enhance their activity against resistant strains of *Plasmodium falciparum* [19]. Remarkably, the presence of functional groups such as fluorine (F), chlorine (Cl), bromine (Br), methoxy (OCH_3), nitro (NO_2), and furan rings into the quinazolinone scaffold has been shown to significantly improve antimalarial efficacy. *In vitro* studies (**Figure 1**) have demonstrated that quinazolinone derivatives bearing these functional groups exhibit IC_{50} values ranging from 1 - 3 µM against *Plasmodium falciparum*, highlighting their potential as effective antimalarial agents [20,21].

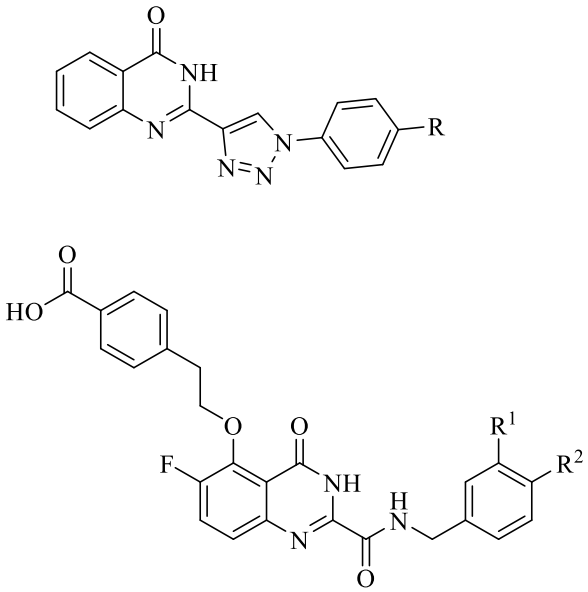

a. R = H, IC_{50} = 2.56 µM
b. R = Cl, IC_{50} = 1.91 µM
c. R = Br, IC_{50} = 1.96 µM
d. R = NO_2, IC_{50} = 1.97 µM

e. R^1 = Et, R^2 = H IC_{50} = 0.42 µM
f. R^1 = OMe, R^2 = F IC_{50} = 1.90 µM
g. R^1 = Me, R^2 = F IC_{50} = 0.59 µM

Figure 1 Quinazolinones with their antiplasmodial activities.

To accelerate the discovery of novel antimalarial compounds, *in silico* methods have become essential tools due to their efficiency and accuracy [22]. Among these, molecular docking, molecular dynamics simulation, and ADMET studies play critical roles in screening and optimizing the best candidate compounds [23]. Molecular docking analyzes the interactions between ligands and key amino acid residues within the

target protein, as well as calculates binding energy to predict binding affinity [24]. Molecular dynamics simulation provides insights into the stability of protein-ligand complexes over time under physiological conditions, allowing evaluation of the flexibility and durability of these interactions [25]. ADMET studies assess the pharmacokinetic properties and safety profiles of drug candidates, which are vital for predicting their behavior in the human body [26].

Several studies summarized in **Table 1** demonstrate a direct correlation between strong interactions at key amino acid residues, favorable binding energy values, and low IC_{50} values obtained from *in vitro* assays. This strong correlation validates *in silico* study as a reliable predictor of biological activity. However, despite these advances, the number of *in silico* studies focused on quinazolinone derivatives as antimalarial agents remains limited. Expanding such computational investigations could offer valuable insights into their potential to inhibit malaria-related proteins and aid in identifying promising new drug candidates for further experimental validation.

Table 1 Computational study of quinazolinone derivatives against several receptors.

Protein	Compound	Key amino acid in hydrogen bond interaction	Binding affinity (kcal/mol)	IC_{50} (µM)	RMSD of MD Simulation (Å)	Ref.
Antimalarial: Falcipain 2 protease (PDB 6SSZ)	**6f**	Gln19	−8.30	*P. falciparum*: 1.91	-	[21]
	JV1	Gln19	−7.30	-	-	
Anticancer: ESR1(PDB 7KBS)	**7h**	Trp102	−8.78	MCF-7: 8.9	-	[27]
	Raloxifene	Trp102	−7.93	-	-	
SARS-CoV-2: 3CLpro (PDB 7K0F)	**5c**	Asn142	−7.50	3CLpro: 1.25	10	[28]
	VR4	Asn142	−9.40	-	20	
Antibacterial: *E. coli* DNA gyrase (PDB 1S14)	**9**	Arg1132	−10.91	*E. coli* DNA gyrase: 2.29	3	[29]
	Novobiocin	Arg1132	−10.78	*E. coli* DNA gyrase: 4.30	1.50	

This study evaluated quinazolinone derivatives as potential *pf*DHFR and *pf*DHODH inhibitors through molecular docking, molecular dynamics simulations, and ADMET analysis. The multi-target approach and predictive analysis employed in this study have not been applied to quinazolinone research before, thus providing new insights into antimalarial drug resistance development. Therefore, the results of this study offer innovative solutions to address the growing challenge of antimalarial drug resistance.

Materials and methods

Materials

The 3-dimensional (3D) single-crystal structures of *P. falciparum*, i.e. *pf*DHFR (PDB: 1J3I) and *pf*DHODH (PDB:1TV5), were obtained from the Protein Data Bank (www.rcsb.org). WR99210 acted as the native ligand for both proteins, with thirty quinazolinones used as ligand models in the study. Computational analyses were carried out on a computer with an Intel® Xeon processor CPU E5-2650 v2@2.60 GHz. The study made use of GaussView 5.0, Gaussian 09W, Chimera 1.13.1, AutoDock 4.2, Discovery Studio 2019, and YASARA software.

Molecular docking analysis

The molecular docking protocol used in this study followed a previously reported procedure with slight modifications [30]. For the redocking analysis, the protein and ligand structures of *pf*DHFR (PDB: 1J3I) and *pf*DHODH (PDB: 1TV5) were prepared using Chimera. The 3D structures of quinazolinone derivatives (**1** - **30**) were generated with GaussView 5.0 and optimized using the DFT B3LYP 6-311G(d,p)

method in Gaussian 09W, except for compound **26**, which was optimized using the AM1 method. The 6-311G(d,p) basis set is not suitable for iodine, as it is designed only for atoms ranging from hydrogen (H) to chlorine (Cl) [31,32]. For optimizing compounds containing iodine, the AM1 method represents a possible alternative [33]. The optimized structures were saved in PDB format. Redocking was conducted with AutoDock4 using a grid box size of 40×40×40 $Å^3$ and 100 runs of the Lamarckian Genetic Algorithm (LGA). The grid box coordinates were set to 27.665, 6.653, and 58.206 (x, y and z) for the *pf*DHFR protein and 38.204, 35.063, and 36.245 (x, y and z) for the *pf*DHODH protein. The method was considered valid for further docking analysis if the RMSD value was below 2 Å. The 2D structures of the quinazolinone derivatives are presented in **Table 1**. The docking of all compounds into the receptor binding sites was performed using the same parameters as those for redocking (grid map size and LGA). The visualization of protein-ligand interactions was carried out using Discovery Studio 2019, focusing on the pose with the lowest binding affinity.

Molecular dynamics simulation

Molecular dynamics simulations for the quinazolinone complexes were conducted using YASARA software. The `md_run.mcr` macro was applied for simulations involving *pf*DHFR (PDB: 1J3I), while `md_runmembrane.mcr` was utilized for *pf*DHODH (PDB: 1TV5). The system employed periodic boundary conditions and the AMBER14 force field. The simulation box dimensions were set to 100×100×100 $Å^3$, with conditions mimicking a physiological environment: Temperature at 310 K, pressure at 1 atm (NPT ensemble), pH 7.4, and 0.9% NaCl. The system underwent energy minimization using the steepest descent approach, followed by simulated annealing minimization, reaching a final density of 0.993 g/mL. A 250 ps equilibration phase was performed to stabilize the system before the production simulations, which ran for 100 ns with a timestep of 2.5 fs. Snapshots were saved every 100 ps. Following simulation, analysis was conducted using Yasara's md_analyze.mcr macro to compute RMSD, RMSF, RoG (Radius of Gyration), SASA (Solvent Accessible Surface Area), and DSSP (Dictionary of Secondary Structure of Proteins) values. The BEcalculation.mcr macro was also used to evaluate MM-PBSA (Molecular Mechanics Poisson-Boltzmann Surface Area) binding energy.

Secondary structure analysis

The 3D protein model was validated through a secondary structure analysis utilizing the RAM (Ramachandran) RAM plot, which assesses the dihedral angles ψ (psi) and φ (phi) of amino acid residues. The RAM plot for the protein under study was acquired from the PDBSum online platform [34].

ADMET study

All compounds were converted into SMILES format using Discovery Studio and then uploaded individually to the pkCSM server [35] and the ProTox-3.0 server [36]. Physicochemical and ADMET properties were analyzed by selecting the ADMET option. The pkCSM server generated data for each compound, including Lipinski's rule of 5, as well as details on absorption, distribution, metabolism, excretion, and toxicity.

Results and discussion

Molecular docking of quinazolinones against *pf*DHFR enzyme

Our study was began with the redocking of the native ligand WR99210 onto the *pf*DHFR enzyme structure from PDB ID 1J3I to validate the molecular docking protocol. The resulting RMSD value was 1.24 Å, which is well within the acceptable threshold of ≤ 2.0 Å for a reliable molecular docking procedure [37]. This indicates that the docking method successfully reproduced the experimental pose of the ligand. The binding energy of WR99210 was calculated to be −5.59 kcal/mol, with a binding constant of 79.47 μM, as shown in **Table 2**, and the superimposed docking pose is visualized in **Figure 2(a)**. These results confirm the validity of the docking protocol and provide a basis for further studies on potential inhibitors targeting *pf*DHFR enzyme.

The redocking of the native ligand revealed key interactions with the *pf*DHFR enzyme. Hydrogen bond interactions were observed with Ile164 (2.20 Å), Ile14 (2.14 Å), and Asp54 (1.83 Å), while hydrophobic interactions involved Pro113, Ile113, Val45, Met55, Phe58, and Leu46. Additionally, a carbon-hydrogen

bond was formed with Ser111 and Ile164. These interactions demonstrated the ligand's strong affinity for the active site of the enzyme. The results highlight the importance of hydrogen bonds and hydrophobic interactions in stabilizing the ligand-enzyme complex, as visualized in **Figure 2(b)**.

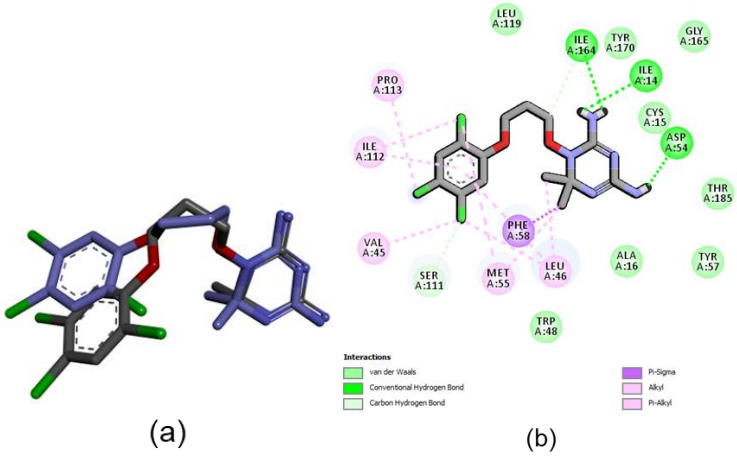

Figure 2 (a) The overlay of WR99210 as the native ligand, displayed in gray before the redocking process and in blue after redocking, (b) The depiction of chemical interactions between WR99210 and the active site of the *pf*DHFR enzyme.

The chemical structures of quinazolinones were optimized by using the DFT-B3LYP 6-311G(d,p) level of theory, a method commonly applied for quinazolinones [38]. Employing this computational approach is crucial for designing effective antimalarial inhibitors, as it accurately models molecular geometry and electronic properties important for binding. It precisely calculates hydrogen-bonding and binding energies, which are key to inhibitor efficacy; strong hydrogen bonds and optimal binding energies improve stability and bioactivity, helping prioritize promising compounds for drug development resistant to parasitic resistance [39,40]. In this study, compound **1** was served as a reference to assess the impact of substituent addition on the inhibitory activity of the proposed quinazolinone derivatives against the *pf*DHFR enzyme.

The docking results of quinazolinone derivatives against the *pf*DHFR enzyme are presented in **Table 2**. Compound **2** exhibits a key hydrogen bond with Ile164 (2.00 Å) and an additional hydrogen bond with Tyr170 (2.19 Å). Unfortunately, its binding energy is only −4.78 kcal/mol, which is not significantly better than the native ligand. To improve the binding energy, modifications were made to the quinazolinone scaffold by adding N-phenyl and C-phenyl groups with various substituents, including hydroxyl (OH), fluorine (F), chlorine (Cl), bromine (Br), methoxy (OCH_3), and nitro (NO_2).

The quinazolinone compounds were designed with phenyl substituents at key positions such as C-2 and N-1 as structure-activity relationship (SAR) studies consistently indicate that these groups are crucial for strong inhibitory activity against enzymes like *pf*DHFR in malaria. The phenyl group at the C-2 position enhances hydrophobic interactions and binding stability within the enzyme's hydrophobic pocket, increasing the inhibitor's potency, while a phenyl group at the N-1 position modulates the electronic and steric properties of the molecule and facilitates π-π stacking with amino acid residues near the active site, both of which are essential for high binding affinity and selectivity. Phenyl substituents were specifically chosen over heterocycles like pyridine or furan because heterocycles can introduce extra polarity or charge that may reduce affinity for the hydrophobic pocket or disrupt the stability of the enzyme-inhibitor complex; furthermore, heterocycles may alter the molecule's electronic and steric characteristics in ways that decrease desired biological activity or cause unwanted side effects, with SAR and docking studies confirming that phenyl groups generally provide superior inhibitory activity and interaction stability. By placing phenyl groups at both

the C and N positions, interactions with different regions of the enzyme's active site are maximized, creating a synergistic effect and strengthening overall binding affinity; this approach is considered more effective than substituting only 1 position, as it ensures optimal inhibitory effects due to more comprehensive interactions [41-44].

This approach proved to be effective. However, only compounds **3**, **5**, and **12** demonstrated hydrogen bond interactions with key amino acid residues. Compound **3** forms a key hydrogen bond with Ile164 (2.10 Å) and an additional hydrogen bond with Ala16 (2.63 Å). It also exhibits hydrophobic interactions with Ile14, Ala16, Cys15, Ile164, and Leu40. This compound has a binding energy of −8.62 kcal/mol and a binding constant of 0.48 μM. Compound **5** forms a key hydrogen bond with Asp54 (1.82 Å) and hydrophobic interactions with Leu40, Leu46, Ala16, Ile14, Phe58, Ile164, Met104, and Ile112. Its binding energy is −8.46 kcal/mol with a binding constant of 0.62 μM. Meanwhile, compound **12** forms a key hydrogen bond with Asp54 (2.23 Å) and an additional hydrogen bond with Ser111 (2.88 Å). It also exhibits hydrophobic interactions with Leu40, Ala16, Ile14, Cys15, Ile164, as well as carbon-hydrogen bonds with Cys15 and Asp54. This compound has a binding energy of −8.49 kcal/mol and a binding constant of 0.59 μM. Based on these data, compound **3** is identified as the best inhibitor against *pf*DHFR due to its superior binding energy compared to the other compounds.

Table 2 The molecular docking results of quinazolinone derivatives in the active site of *pf*DHFR (PDB: 1J3I).

Molecule ID	Structure	Binding energy (kcal/mol)	Binding Constant (μM)	RMSD (Å)	Type of Interaction		
					H-bond (Å)	Hydrophobic	Others
WR99210	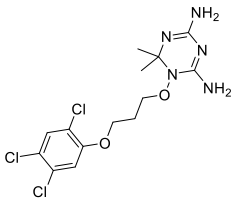	−5.59	79.47	1.24	Ile164 (2.20), Ile14 (2.14), Asp54 (1.83)	Pro113, Ile112, Val45, Met55, Phe58, Leu46	Carbon Hydrogen Bond: Ser111, Ile164
1	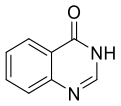	−4.78	315.80	0.10	Tyr170 (2.19), Ile164 (2.00)	Ala16, Ile14, Phe58, Ile164	-
2	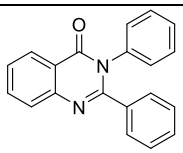	−8.40	0.70	0.89	Ala16 (2.33)	Leu40, Ile14, Phe58, Ala16, Ile164	Pi-Sulfur: Met55
3	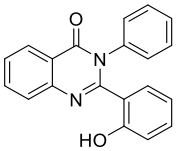	−8.62	0.48	0.19	Ala16 (2.63), Ile164 (2.10)	Ile14, Ala16, Cys15, Ile164, Leu40	-
4	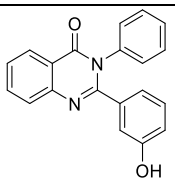	−8.55	0.54	0.23	Ala16 (2.15)	Ile14, Leu40, Ala16, Leu46, Ile112	Pi-Sulfur: Met55

Molecule ID	Structure	Binding energy (kcal/mol)	Binding Constant (μM)	RMSD (Å)	Type of Interaction		
					H-bond (Å)	Hydrophobic	Others
5	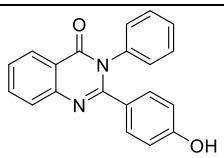	−8.46	0.62	0.23	Asp54 (1.82)	Leu40, Leu46, Ala16, Ile14, Phe58, Ile164, Met104, Ile112	-
6	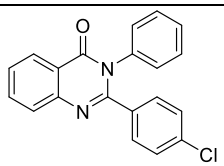	−8.84	0.33	0.37	Ser111 (3.08)	Leu40, Ala16, Phe58, Cys15, Ile14, Ile164	-
7	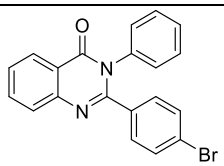	−9.13	0.20	0.10	Ser111 (3.09)	Leu40, Phe58, Ala16, Cys15, Ile14, Ile164	-
8	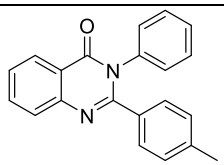	−8.64	0.46	0.26	Ser111 (3.06)	Leu40, Ala16, Phe58, Cys15, Ile14, Ile164	-
9	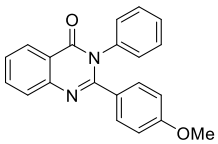	−8.74	0.39	0.16	Ser111 (2.95)	Leu40, Ala16, Cys15, Ile14, Ile164	Carbon Hydrogen Bond: Cys15, Asp54
10	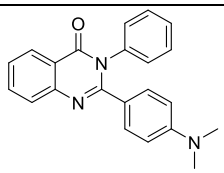	−8.40	0.70	0.33	-	Leu40, Ile164, Ala16, Ile14, Cys15	-
11	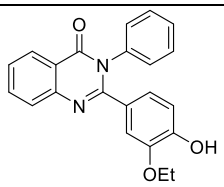	−8.48	0.61	0.32	Ala16 (2.52)	Leu40, Met55, Phe58, Ile14, Cys15, Ala16	Pi-Sulfur: Met55
12	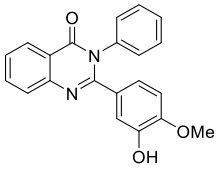	−8.49	0.59	0.39	Ser111 (2.88), Asp54 (2.23)	Leu40, Ala16, Ile14, Cys15, Ile164	Carbon Hydrogen Bond: Cys15, Asp54
13	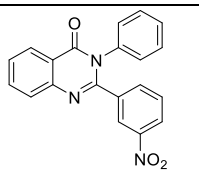	−8.74	0.39	0.26	Ala16 (2.45)	Leu40, Ile14, Cys15, Ala16, Leu46	Pi-Sulfur: Met55

Molecule ID	Structure	Binding energy (kcal/mol)	Binding Constant (μM)	RMSD (Å)	Type of Interaction		
					H-bond (Å)	Hydrophobic	Others
14	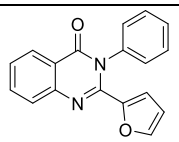	−7.83	1.81	0.64	Ala16 (2.28)	Leu40, Ile164, Cys15, Ala16, Ile14	-
15	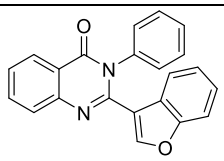	−8.91	0.30	0.46	Ala16 (2.45)	Leu40, Phe58, Ile164, Ala16, Ile14	Carbon Hydrogen Bond: Ile164
16	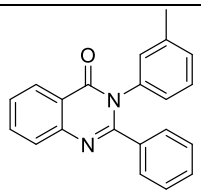	−8.46	0.63	0.18	Ser111 (3.08)	Leu40, Ile14, Cys15, Ala16, Phe58, Ile164, Met55	-
17	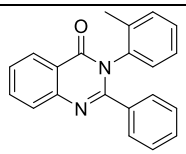	−8.88	0.31	0.19	Ala16 (2.28)	Leu40, Ile164, Cys15, Ala16, Leu46, Ile14, Trp48	Pi-Sulfur: Met55
18	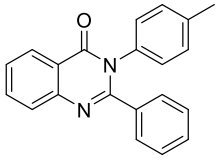	−9.03	0.24	0.08	Ala16 (2.39)	Leu40, Ile164, Ile14, Cys15, Ala16, Phe58	Pi-Sulfur: Met55
19	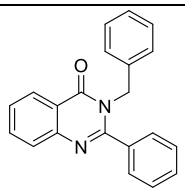	−8.15	1.06	0.11	Ser111 (2.24)	Leu40, Ala16, Leu46, Cys15, Ile164, Ile112	Pi-Sulfur: Met104
20	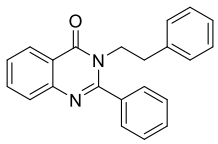	−8.68	0.43	0.72	Ser111 (2.77)	Cys15, Ala16, Ile164	Carbon Hydrogen Bond: Ile164
21	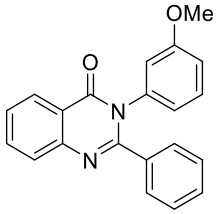	−8.31	0.80	0.35	Ser108 (2.62)	Leu40, Ile14, Cys15, Phe58, Ala16, Ile164	-
22	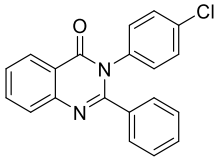	−9.19	0.18	0.88	Ala16 (2.68)	Leu40, Ile164, Ile14, Cys15, Ala16, Phe58	-

Molecule ID	Structure	Binding energy (kcal/mol)	Binding Constant (μM)	RMSD (Å)	Type of Interaction		
					H-bond (Å)	Hydrophobic	Others
23	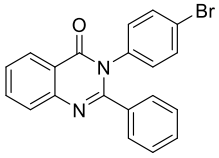	−9.41	0.13	0.18	-	Leu40, Ile164, Ile14, Cys15, Ala16, Phe58	-
24	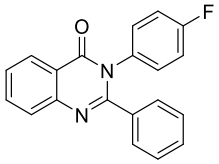	−8.35	0.75	0.54	Ala16 (2.57)	Leu40, Ile164, Cys15, Ala16, Ile14	Pi-Sulfur: Met55 Halogen (Fluorine): Asp54
25	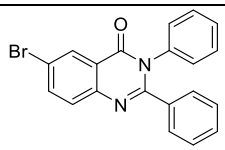	−8.73	0.40	0.19	Ser111 (2.96)	Val195, Leu40, Ile14, Ala16, Ile164	-
26	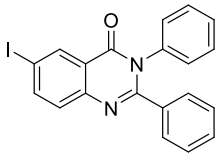	−9.04	0.23	0.22	Ser111 (3.10)	Val195, Leu40, Ile14, Ala16, Cys15, Ile164	-
27	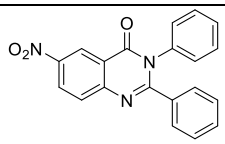	−9.21	0.18	0.2	Arg122 (1.82)	Leu119, Met55, Leu46, Ile112	Pi-Sulfur: Met55
28	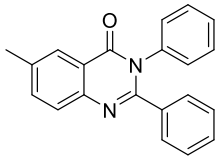	−8.55	0.54	1.45	-	Ile164, Cys15, Ala16, Ile14, Leu40, Val195	-
29	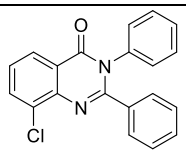	−8.75	0.39	0.51	Ala16 (2.43)	Ile164, Cys15, Ala16, Phe58, Ile14, Leu40	Pi-Sulfur: Met55
30	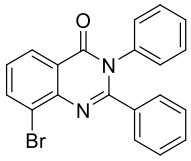	−8.91	0.29	0.23	Ala16 (2.29)	Ile164, Cys15, Ala16, Ile14, Leu40	Pi-Sulfur: Met55

Molecular docking of quinazolinones against *pf*DHODH enzyme

Redocking was performed using the native ligand A26 against the *Pf*HODH enzyme with the PDB ID 1TV5. The resulting RMSD value was 1.70 Å, with the superimposed pose shown in **Figure 3(a)**. Additionally, the binding energy was calculated to be −5.06 kcal/mol, and the binding constant was determined to be 193.88 μM, as presented in **Table 3**. Key hydrogen bonds were observed with Met536 (2.54 Å), Arg265 (1.88 Å), and His (1.91 Å). Hydrophobic interactions were identified with Leu172, Cys175, Phe188, Cys184, and Val532, while Carbon-Hydrogen bonds were formed with Gly535 and Gly181. Furthermore, a halogen interaction (fluorine) was noted with Gly535. These interactions are visualized in **Figure 3(b)**.

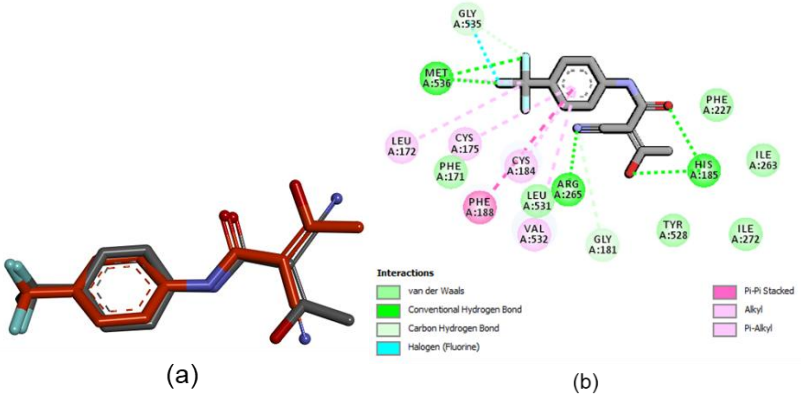

Figure 3 (a) The overlay of A26 as the native ligand, displayed in gray before the redocking process and in red after redocking, (b) The depiction of chemical interactions between A26 and the active site of the *pf*DHODH enzyme.

Docking of quinazolinone derivatives was performed at the same binding site as A26, the native ligand. The docking results for the *pf*HODH enzyme are summarized in **Table 3**. Compound **1** exhibited key hydrogen bond interactions with the amino acids Arg265 (2.41 Å) and His185 (2.05 Å), along with an additional hydrogen bond with Gly181 (2.30 Å). Furthermore, it demonstrated hydrophobic interactions with Val532 and Cys184, as well as a Pi-donor hydrogen bond with Cys184. This compound showed a binding energy of −5.54 kcal/mol, which is better than that of the native ligand, and a binding constant of 86.94 µM.

Modifications to the quinazolinone framework were implemented to enhance binding energy by incorporating N-phenyl and C-phenyl groups with various substituents, including hydroxyl (OH), fluorine (F), chlorine (Cl), bromine (Br), methoxy (OCH_3), and nitro (NO_2). All proposed compounds exhibited key interactions similar to the native ligand A26. Among these, compounds **2**, **11**, and **20** demonstrated the most promising results. Compound **2** showed a binding energy of −9.59 kcal/mol, with a binding constant of 0.09 µM and an RMSD of 0.26 Å. It formed crucial hydrogen bonds with Arg265 and His185, similar to the native ligand, and hydrophobic interactions with Ile263, Leu531, Val532, Cys175, Leu176, and Cys184. Additionally, it engaged in Carbon Hydrogen Bond, Pi-Donor Hydrogen Bond, and Pi-Sulfur interactions with Cys184. Compound **11** had a binding energy of −10.12 kcal/mol, a binding constant of 0.04 µM, and an RMSD of 0.87 Å. It shared hydrogen bonding with Arg265, similar to the native ligand, and hydrophobic interactions with Ile263, Val532, Phe188, Leu531, Phe171, Met536, Leu172, Leu176, Cys175, and Cys184. It also formed Carbon Hydrogen Bond and Pi-Donor Hydrogen Bond interactions with Cys184 and Gly181, as well as a Pi-Sulfur interaction with Cys184. Compound **20** exhibited a binding energy of −9.96 kcal/mol, a binding constant of 0.11 µM, and an RMSD of 0.24 Å. It formed hydrogen bonds similar to the native ligand with His185 and Arg265, and hydrophobic interactions with Ile263, Cys184, Val532, Leu531, and Leu172. It also engaged in Pi-Sulfur interactions with Cys184 and Cys175. These findings highlight the potential of these compounds as effective ligands due to their strong interactions with the target protein.

Table 3 The molecular docking results of quinazolinone derivatives in the active site of *pf*DHODH (PDB: 1TV5).

Molecule ID	Structure	Binding energy (kcal/mol)	Binding Constant (μM)	RMSD (Å)	Type of Interaction		
					H-bond (Å)	Hydrophobic	Others
1	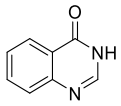	−5.54	86.94	0.98	Arg265 (2.41), Gly181 (2.30), His185 (2.05)	Val532, Cys184	Pi-Donor Hydrogen Bond: Cys184
2	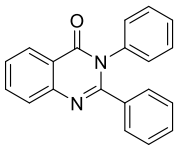	−9.59	0.09	0.26	Arg265 (1.90), His185 (2.04)	Ile263, Leu531, Val532, Cys175, Leu176, Cys184	Carbon Hydrogen Bond, Pi- Donor Hydrogen Bond, and Pi-Sulfur: Cys184
3	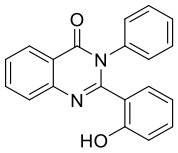	−8.81	0.35	0.17	His185 (2.25), Val532 (2.00)	Val532, Leu172, Cys184	Pi-Donor Hydrogen Bond: Cys175 Pi-Lone Pair: Leu531
4	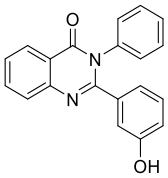	−9.46	0.12	0.27	Arg265 (2.02), Leu531 (2.10)	Ile263, Val532, Cys184, Cys175, Leu176	Carbon Hydrogen Bond, Pi- Donor Hydrogen Bond, and Pi-Sulfur: Cys184
5	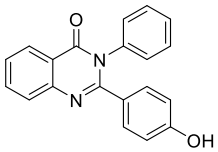	−8.61	0.49	0.11	Arg265 (1.84)	Ile263, Val532, Cys184, Leu176, Cys175	Carbon Hydrogen Bond, Pi- Donor Hydrogen Bond, and Pi-Sulfur: Cys184
6	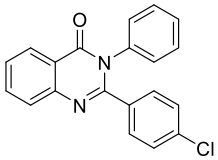	−8.84	0.33	0.24	Arg265 (1.76)	Ile263, Val532, Phe188, Met536, Cys184, Leu176, Cys175	Carbon Hydrogen Bond, Pi- Donor Hydrogen Bond, and Pi-Sulfur: Cys184
7	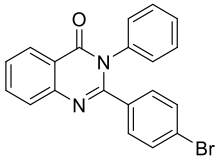	−8.25	0.89	0.14	Arg265 (1.71)	Ile263, Val532, Phe188, Met536, Cys184, Cys175, Leu176	Carbon Hydrogen Bond and Pi-Donor Hydrogen Bond and Carbon Hydrogen Bond: Gly181, Cys184 Pi-Sulfur: Cys184

Molecule ID	Structure	Binding energy (kcal/mol)	Binding Constant (μM)	RMSD (Å)	Type of Interaction		
					H-bond (Å)	Hydrophobic	Others
8	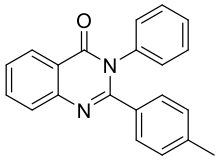	−9.09	0.22	0.23	Arg265 (1.82)	Leu176, Cys175, Cys184, Phe188, Met536, Val532, Ile263	Carbon Hydrogen Bond, Pi-Donor Hydrogen Bond, and Pi-Sulfur: Cys184
9	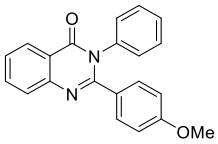	−9.07	0.23	0.19	Arg265 (1.84), His185 (2.01)	Ile263, Val532, Leu531, Cys184, Cys175, Leu176	Carbon Hydrogen Bond, Pi-Donor Hydrogen Bond, and Pi-Sulfur: Cys184
10	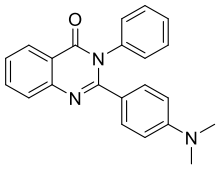	−9.12	0.20	0.15	Arg265 (1.77), His185 (2.02)	Ile263, Val532, Cys184, Cys175, Leu176	Carbon Hydrogen Bond and Pi-Donor Hydrogen Bond: Cys184, Leu531 Pi-Sulfur: Cys184
11	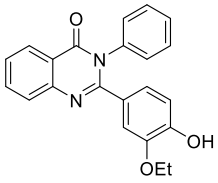	−10.12	0.04	0.87	Arg265 (1.77)	Ile263, Val532, Phe188, Leu531, Phe171, Met536, Leu172, Leu176, Cys175, Cys184	Carbon Hydrogen Bond and Pi-Donor Hydrogen Bond: Cys184, Gly181 Pi-Sulfur: Cys184
12	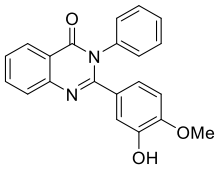	−8.91	0.30	0.21	Arg265 (1.84), Leu531 (2.31), His185(2.21)	Ile263, Val532, Leu176, Cys175	Carbon Hydrogen Bond, Pi-Donor Hydrogen Bond, and Pi-Sulfur: Cys184
13	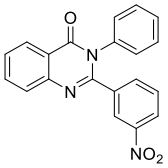	−9.39	0.13	0.29	Arg265 (1.88), His185 (2.17), Cys184 (3.27)	Ile263, Val532, Cys184, Leu176, Cys175	Carbon Hydrogen Bond, Pi-Donor Hydrogen Bond, and Pi-Sulfur: Cys184
14	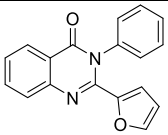	−9.31	0.15	1.36	His185 (1.68), Arg265 (2.99)	Ile263, Val532, Cys184, Cys175, Leu176	Carbon Hydrogen Bond and Pi-Sulfur:
15	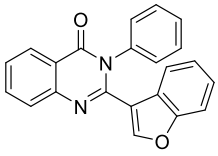	−9.46	0.12	0.26	Arg265 (2.01)	Ile263, Leu531, Cys175, Leu176, Val532	Carbon Hydrogen Bond, Pi-Donor Hydrogen Bond, and Pi-Sulfur: Cys184

Molecule ID	Structure	Binding energy (kcal/mol)	Binding Constant (μM)	RMSD (Å)	Type of Interaction		
					H-bond (Å)	Hydrophobic	Others
16	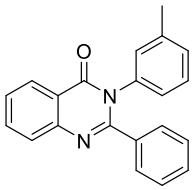	−9.28	0.16	0.43	Arg265 (1.99), His185 (2.04)	Ile265, Val532, Leu531, Leu172, Cys175, Leu176, Cys184	Carbon Hydrogen Bond, Pi-Donor Hydrogen Bond, and Pi-Sulfur: Cys184
17	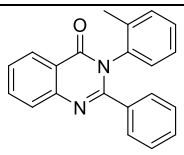	−8.86	0.32	0.11	Arg265 (2.90), Cys184 (2.75)	Val532, Cys175, Cys184, Leu172, Leu176, Phe188	Pi-Lone Pair: Leu531
18	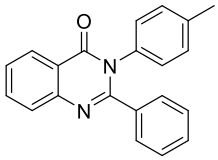	−8.71	0.41	1.29	His185 (2.06)	Val532, Cys184, Cys175, Leu172, Leu176, Phe188, Met536, Leu240, Ile263	-
19	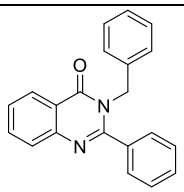	−8.87	0.31	0.11	His185 (1.66)	Val532, Cys184, Leu176, Cys175, Leu172, Leu531, Phe188	Pi-Donor Hydrogen Bond: Cys184
20	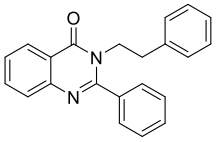	−9.96	0.05	0.24	Arg265 (2.08), His185 (2.14)	Ile263, Cys184, Val532, Leu531, Leu172	Pi-Sulfur: Cys184, Cys175
21	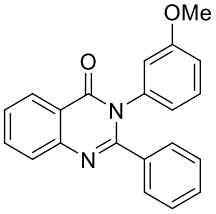	−9.48	0.11	1.68	His185 (1.71), Arg265 (2.93)	Ile263, Val532, Cys184, Leu176, Cys175, Leu172	Carbon Hydrogen Bond, Pi-Donor Hydrogen Bond, and Pi-Sulfur: Cys184
22	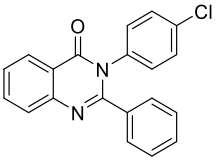	−8.69	0.42	0.26	His185 (1.57)	Ile263, Val532, Leu176, Cys175, Cys184, Met536, Phe188, Ile272	Pi-Donor Hydrogen Bond and Pi-Sulfur: Cys184
23	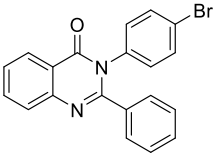	−8.06	1.24	1.36	His185 (1.87)	Ile263, Val532, Cys184, Leu176, Leu172, Cys175, Leu240, Phe188, Met536, Leu531	-
24	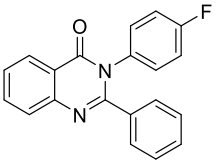	−9.03	0.24	0.16	Arg265 (1.92), Leu176 (2.44), His185 (2.09)	Ile263, Leu531, Val532, Cys175, Leu176, Cys184	Carbon Hydrogen Bond, Pi-Donor Hydrogen Bond, and Pi-Sulfur: Cys184

Molecule ID	Structure	Binding energy (kcal/mol)	Binding Constant (μM)	RMSD (Å)	Type of Interaction		
					H-bond (Å)	Hydrophobic	Others
							Halogen (Fluorine): Leu172, Cys175
25	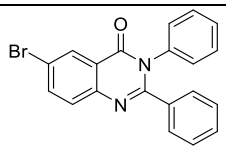	−8.35	0.75	0.36	His185 (2.52), Cys184 (2.83)	Tyr528, Val532, Cys184, Leu172, Leu531, Ile263	Pi-Donor Hydrogen Bond: Cys175
26	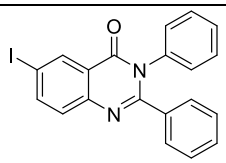	−7.87	1.69	0.12	His185 (2.76), Cys184 (2.63)	Tyr528, Val532, Cys184, Leu172, Phe188, Met536, Leu531, Ile263	Pi-Donor Hydrogen Bond: Cys175
27	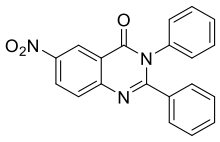	−8.98	0.26	0.39	His185 (1.56), Arg265 (2.97)	Ile272, Ile263, Leu172, Val532, Cys184, Cys175, Leu176	Carbon Hydrogen Bond, Pi-Donor Hydrogen Bond, and Pi-Sulfur: Cys184
28	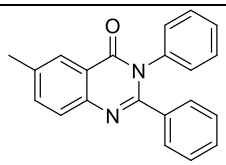	−8.94	0.28	0.11	His185 (2.14)	Ile263, Tyr528, Val532, Cys184, Leu176, Cys175, Leu172, Leu531	-
29	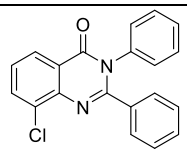	−8.95	0.28	0.22	His185 (1.56)	Ile272, Ile263, Arg265, Val532, Cys175, Leu176, Cys184	Pi-Donor Hydrogen Bond, Pi-Sulfur: Cys184
30	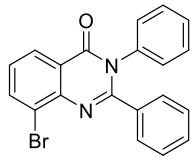	−8.26	0.88	0.17	His185 (1.72)	Ile263, Arg265, Val532, Cys184, Leu176, Cys175	Carbon Hydrogen Bond and Pi-Donor Hydrogen Bond: Gly181, Cys184 Pi-Sulfur: Cys184
A26	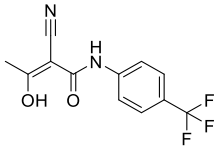	−5.06	193.88	1.70	Met536 (2.54), Arg265 (1.88), His 185 (1.91)	Leu172, Cys175, Phe188, Cys184, Val532	Carbon Hydrogen Bond: Gly535, Gly181 Halogen (Fluorine): Gly535

Molecular dynamics simulations against *pf*DHFR and *pf*DHODH protein

The molecular dynamics simulations provided valuable insights into the stability and binding efficacy of selected quinazolinone derivatives against the targets *pf*DHFR and *pf*DHODH. From the molecular docking studies, 3 promising compounds were identified for each protein target. RMSD analysis, presented in **Figure 4**, further elucidated the dynamic behavior of these protein-ligand complexes throughout the simulation period.

Notably, compound **12** exhibited a backbone RMSD of 3.07 ± 0.58 Å, which is higher than those of compound **3** (2.17 ± 0.23 Å), compound **5** (2.12 ± 0.28

Å), and the native ligand (2.16 ± 0.25 Å). Generally, an RMSD value below **3** Å indicates a stable protein-ligand complex, suggesting that compounds with lower RMSD values maintain more stable interactions during the simulation.

For *pf*DHODH inhibition, compound **20** showed an average RMSD of 2.05 ± 0.21 Å, which was lower than compound **2** (2.28 ± 0.25 Å), compound **11** (2.20 ± 0.13 Å), and the native ligand (2.33 ± 0.56 Å). These findings imply that compounds **3** and **5** provide greater structural stability when bound to *pf*DHFR, while compounds **20**, **2**, and **11** display comparable stability toward *pf*DHODH.

The relatively consistent and low RMSD values across these compounds highlight their potential as effective inhibitors for further antimalarial drug development [45]. Structural stability is critical because it reflects the ability of a compound to maintain a stable binding conformation over time, which often correlates with sustained inhibition and better therapeutic efficacy [46]. Therefore, these RMSD results reinforce the significance of dynamic stability as a key parameter guiding the selection of promising drug candidates targeting these enzymes.

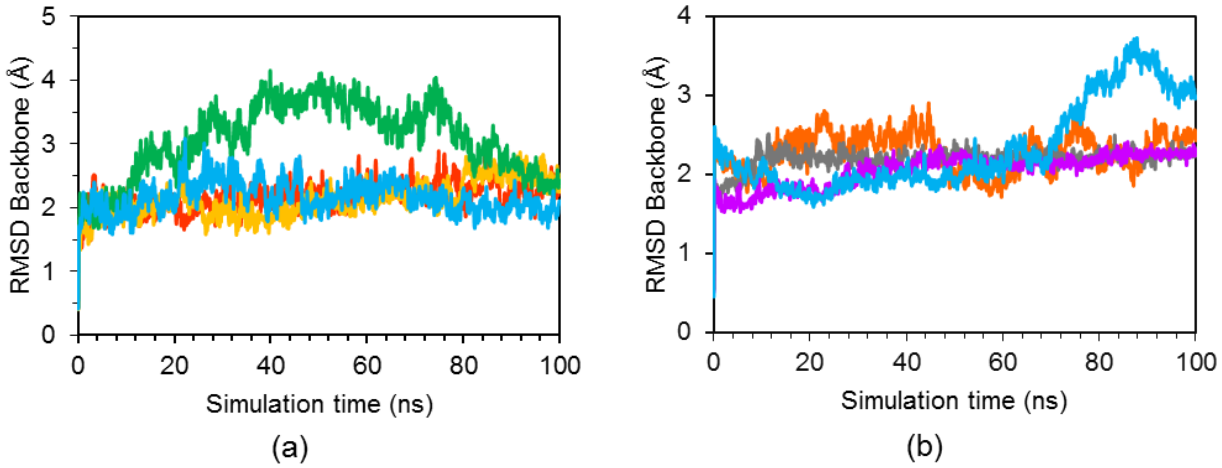

Figure 4 RMSD of the backbone for (a) compound **3** (red line), compound **5** (yellow line), compound **12** (green line), and WR99210 (blue line) against *pf*DHFR and for (b) compound **2** (orange line), compound **11**(grey line), compound **20** (purple line), and A26 (blue line) against *pf*DHODH.

The analysis of RMSF values for the protein-ligand complexes provided valuable insights into the flexibility and stability of the systems. RMSF analysis was also performed as shown in **Figure 5**. For *pf*DHFR, the RMSF values were as follows: Compound **3** exhibited an RMSF of 1.60 ± 1.10 Å, compound **5** showed an RMSF of 1.62 ± 1.11 Å, and compound **12** had an RMSF of 1.76 ± 1.43 Å, while the native ligand displayed an RMSF of 1.57 ± 1.04 Å. Notably, certain residues (1 - 3, 25 - 34, 43 - 45, 85 - 97, 115, 116, 132 - 139, and 230 - 233) demonstrated RMSF values exceeding 2 Å, indicating higher flexibility in these regions.

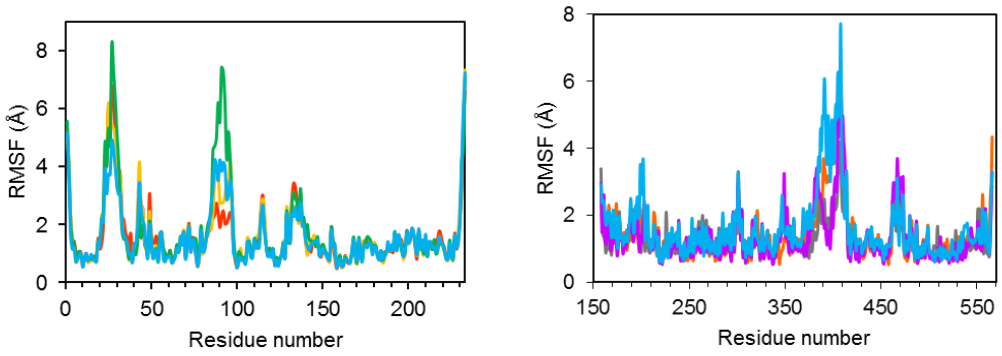

Figure 5 RMSF (a) compound **3** (red line), compound 5 (yellow line), compound **12** (green line), and WR99210 (blue line) against *pf*DHFR and (b) compound **2** (orange line), compound **11**(grey line), compound **20** (purple line), and A26 (blue line) against *pf*DHODH.

In contrast, for *pf*DHODH, the RMSF values were: compound **2** had an RMSF of 1.41 ± 0.82 Å, compound 11 showed an RMSF of 1.29 ± 0.54 Å, compound **20** exhibited an RMSF of 1.36 ± 0.78 Å, and the native ligand displayed an RMSF of 1.59 ± 0.98 Å. Specific residues (159 - 161, 166, 171, 199, 203, 301, 302, 376 and 383 - 414) in *pf*DHODH also exhibited RMSF values greater than 2 Å, highlighting regions of increased flexibility within this enzyme. These findings suggest that although the ligands generally stabilize the protein structures, certain regions remain relatively flexible, which could influence binding dynamics and enzymatic function. Understanding these flexible regions is essential because they may affect the overall efficacy and mechanism of inhibition of these potential antimalarial compounds.

Further RAM analysis was also performed as shown in **Figure 6**. The *pf*DHFR complexed with compound **3** generated the most favored regions with 192 residues (88.1%), additional allowed regions with 26 residues (11.9 %), generously allowed regions with 0 residues (0%), and disallowed regions with 0 residues (0%). Meanwhile, the *pf*DHFR complexed with compound **5** generate the most favored regions with 185 residues (84.9%), additional allowed regions with 31 residues (14.2%), generously allowed regions with 2 residues (0.9%), and disallowed regions with 0 residues (0%). Moreover, the *Pf*DHFR complexed with compound **12** generate the most favored regions with 191 residues (87.6%), additional allowed regions with 23 residues (10.6%), generously allowed regions with 2 residues (0.9%), and disallowed regions with 2 residues (0.9%). These results revealed that almost all regions of *pf*DHFR complexed with quinazolinones were located in allowed regions according to the RAM plot. The DSSP of each ligand in the active site of *pf*DHFR agreed with the RAM data that each helix, sheet, turn, coil, helix310, and helixPi fractions of *pf*DHFR remains stable during the 100 ns molecular dynamics simulations as shown in **Figure 7**.

The *pf*DHODH complexes with compounds **2**, **11**, and **20** exhibited favorable structural characteristics based on RAM plot analysis in **Figure 6**. Specifically, the complex with compound **2** showed 325 residues (87.8%) in the most favored regions, 41 residues (11.1%) in additional allowed regions, 3 residues (0.8%) in generously allowed regions, and 1 residue (0.3%) in disallowed regions. The complex with compound **11** had 326 residues (88.1%) in the most favored regions, 43 residues (11.6%) in additional allowed regions, and 1 residue (0.3%) in disallowed regions, with no residues in generously allowed regions. Meanwhile, the complex with compound **20** featured 318 residues (85.9%) in the most favored regions, 48 residues (13.0%) in additional allowed regions, 2 residues (0.5%) in generously allowed regions, and 2 residues (0.5%) in disallowed regions. These results indicate that nearly all regions of *pf*DHODH complexed with quinazolinones fell within allowed regions according to the RAM plot. Furthermore, the Dictionary of Secondary Structure of Proteins (DSSP) analysis for each ligand in the *pf*DHODH active site supported the RAM data, showing that the fractions of helices, sheets, turns, coils, helix310, and helixPi in *pf*DHODH remained stable throughout the 100 ns molecular dynamics simulations.

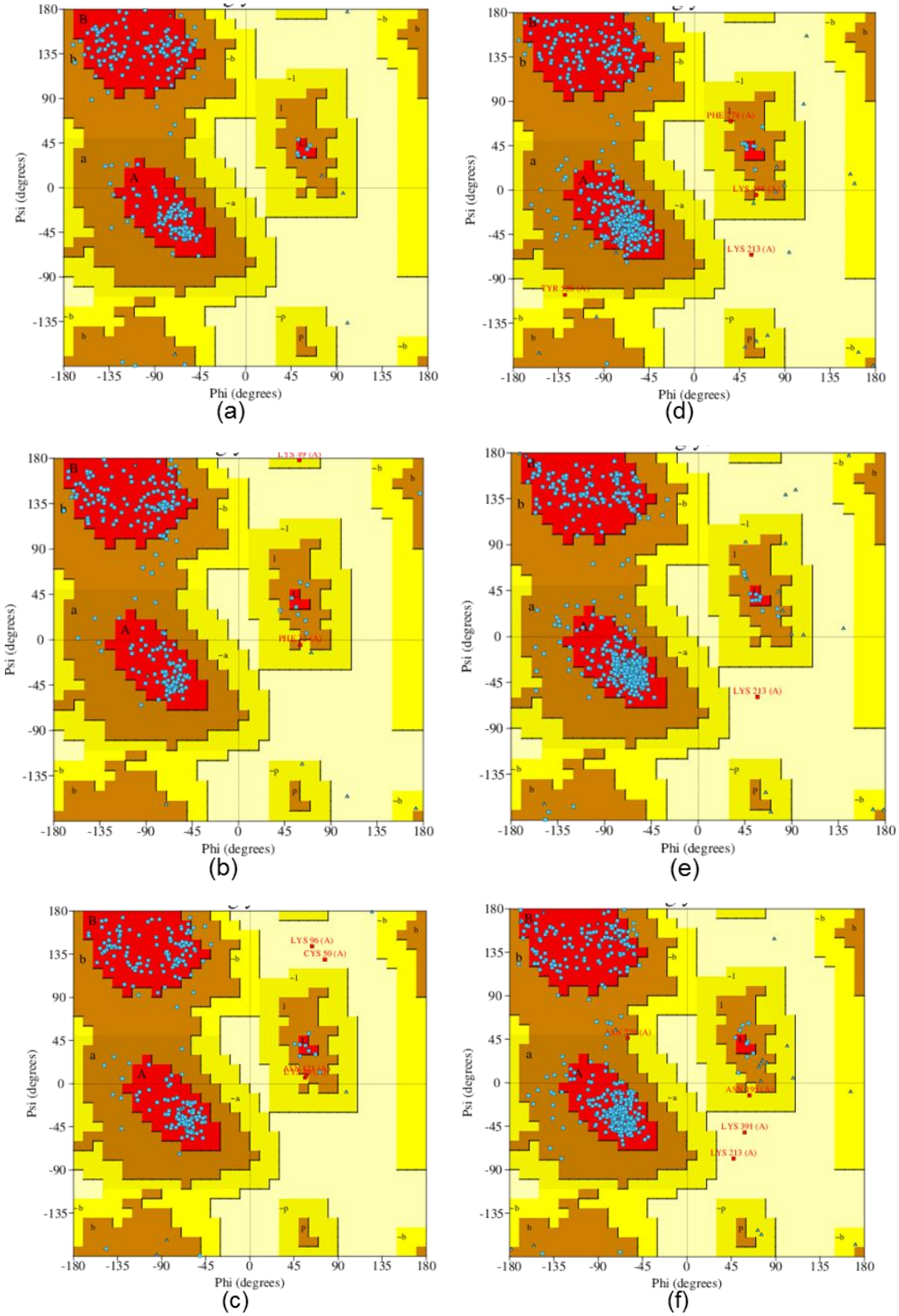

Figure 6 RAM plot for (a) compound **3**, (b) compound **5**, and (c) compound 12 against *pf*DHFR and for (d) compound 2, (e) compound 11, and (f) compound 20 against *pf*DHODH.

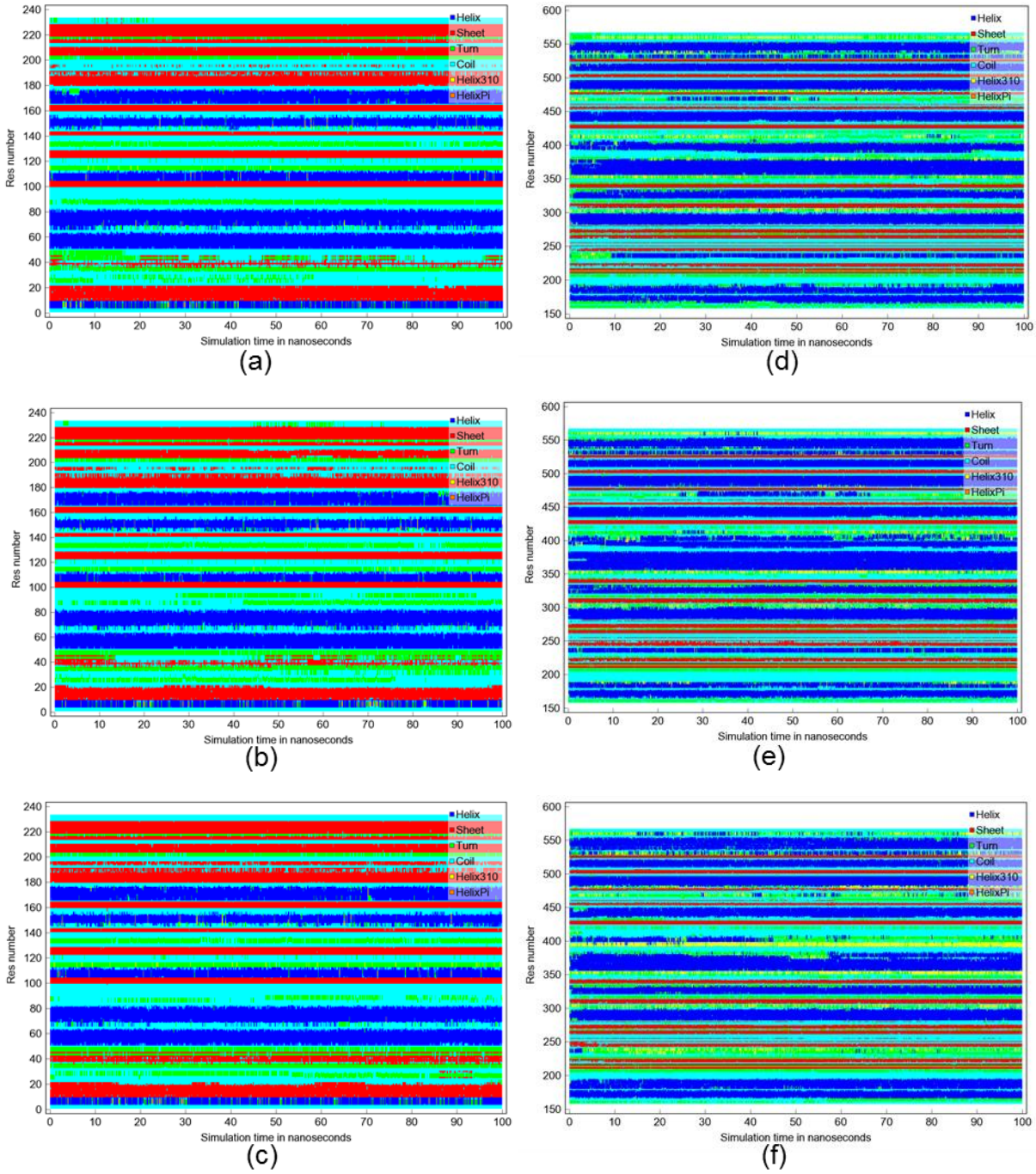

Figure 7 DSSP analysis for (a) compound **3**, (b) compound **5**, and (c) compound 12 against *pf*DHFR and for (d) compound 2, (e) compound 11, and (f) compound 20 against *pf*DHODH.

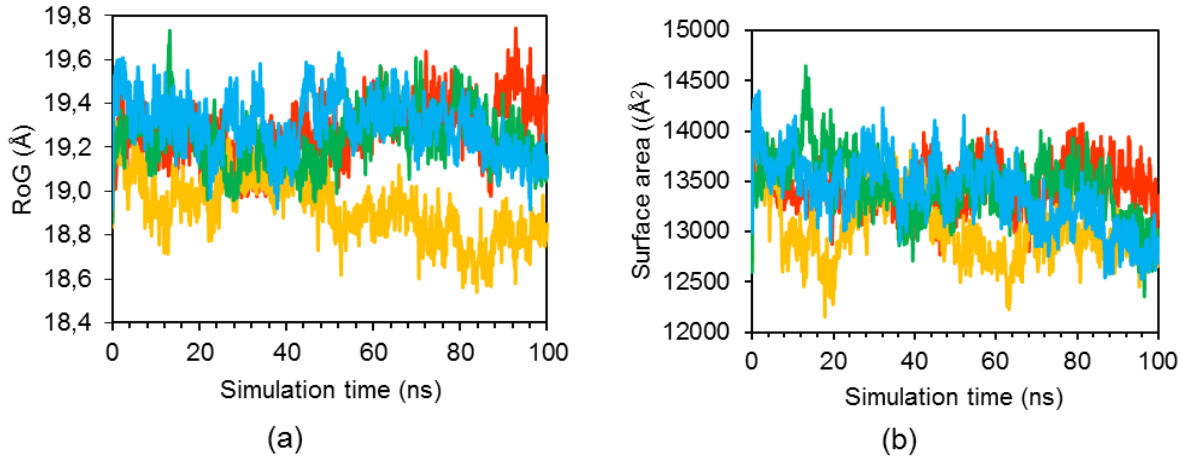

Figure 8 (a) RoG of the backbone and (b) SASA during 100 ns simulation for compound 3 (red line), compound 5 (yellow line), compound 12 (green line), and WR99210 (blue line) against *pf*DHFR.

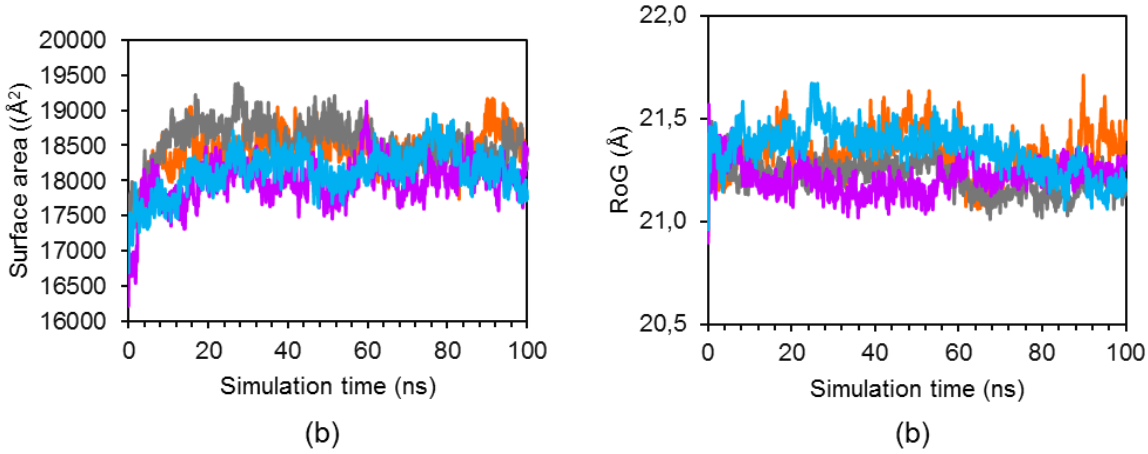

Figure 9 (a) RoG of the backbone and (b) SASA during 100 ns simulation for compound 2 (orange line), compound 11(grey line), compound 20 (purple line), and A26 (blue line) against *pf*DHODH.

The compactness of the *pf*DHFR protein complexed with quinazolinones is effectively captured by the RoG values. As illustrated in **Figure 8**, the RoG values for compounds **3**, **5**, **12**, and **WR99210** were determined to be 19.28 ± 0.13, 18.92 ± 0.14, 19.25 ± 0.12 and 19.30 ± 0.13 Å, respectively. These values remained relatively stable and did not exhibit significant differences throughout the molecular dynamics simulations. Additionally, the SASA values, also presented in **Figure 8**, provide insight into the accessible surface area of the *pf*DHFR protein complex for each ligand. The SASA data for compounds **3**, **5**, **12**, and **WR99210** were found to be 13,444 ± 222, 13,016 ± 323, 13,447 ± 305 and 13,390 ± 346 Å^2, respectively. These SASA values align with the stable RoG values, indicating that both metrics support the overall stability of the *pf*DHFR complexes during the simulations.

Additionally, the RoG values of *pf*DHODH protein complexed with quinazolinones of compound **2**, **11**, **20** and **A26** were 21.30 ± 0.11, 21.20 ± 0.08, 21.20 ± 0.07 and 21.40 ± 0.11 Å, respectively. These values were not significantly different and relatively stable during the molecular dynamics simulations. On the other hand, SASA value represent the accessible surface area of *pf*DHODH protein complex for each ligand. As presented in in **Figure 9(b)**, The SASA data of compound **2**, **11**, **20** and **A26** were 18,431 ± 288, 18,537 ± 306, 17,987 ± 309, and 18,127 ± 308 Å^2. These values were in line with the RoG value was stable during the molecular dynamics simulations.

The energy calculations for the *pf*DHFR complexes with compounds **3**, **5, 12**, and **WR99210** provide valuable insights into their binding characteristics (**Table 4**). The potential energy of the receptor-ligand interactions (EpotRecept+) showed that **WR99210** had the most favorable value at −338.92 ± 22.50 kJ/mol, followed by compound **3** at −153.63 ± 21.28 kJ/mol. The desolvation energy of the receptor (EsolvRecept+) highlighted significant differences, with WR99210 having the most negative value at −488.52 ± 23.66 kJ/mol, indicating strong interactions. The ligand's potential energy (EpotLigand+) and desolvation energy (EsolvLigand-) also varied, reflecting distinct binding modes. Notably, the calculated binding energies revealed that **WR99210** exhibited the most favorable binding energy at −141.81 ± 47.72 kJ/mol, while compound **12** had a positive binding energy, suggesting less favorable interactions. Overall, these energy calculations suggest that **WR99210** forms the most stable complex with *pf*DHFR, followed by compounds **5** and **3**, with compound **12** being less stable.

Table 4 MM-PBSA calculation for compounds **3**, **5**, **12**, and WR99210 after molecular dynamics simulations in the active site of *pf*DHFR.

Energy	Energy value (kJ/mol)			
	3	**5**	**12**	**WR99210**
EpotRecept+	−153.63 ± 21.28	−131.97 ± 18.84	−64.27 ± 19.87	−338.92 ± 22.50
EsolvRecept+	−62.10 ± 14.88	−94.33 ± 8.85	−89.49 ± 9.27	−488.52 ± 23.66
EpotLigand+	−3,628.44 ± 613.85	−4,252.03 ± 629.34	−3,717.26 ± 668.07	−3,989.22 ± 756.09
EsolvLigand−	−27,542.09 ± 2,411.74	−26,324.16 ± 1,338.50	−27,330.16 ± 1,030.85	−26,874.55 ± 1,311.99
EpotComplex−	−3,980.83 ± 615.12	−4,630.00 ± 630.73	−3,952.08 ± 670.60	−4,820.87 ± 745.44
EsolvComplex	−27,397.93 ± 2,413.33	−26,162.13 ± 1,343.53	−27278.49 ± 1,027.60	−26,728.53 ± 1,293.07
Binding energy	−7.65 ± 23.26	−10.47 ± 33.50	29.73 ± 30.93	−141.81 ± 47.72

The energy calculations for the *pf*DHODH complexes with compounds **2**, **11**, **20**, and **A26** offer insights into their binding properties (**Table 5**). The potential energy of the receptor-ligand interactions (EpotRecept+) showed that compound **11** had the most favorable value at −99.25 ± 21.07 kJ/mol, while compound 2 and compound **20** had less favorable values. The desolvation energy of the receptor (EsolvRecept+) highlighted significant differences, with compound **11** having the most negative value at −67.21 ± 9.52 kJ/mol, indicating strong interactions. The ligand's potential energy (EpotLigand+) and desolvation energy (EsolvLigand−) varied, reflecting distinct binding modes. Notably, the calculated binding energies revealed that all compounds had positive values, with **A26** exhibiting the highest at 156.70 ± 28.77 kJ/mol, suggesting less favorable interactions compared to negative binding energies typically associated with stable complexes. Overall, these energy calculations suggest that while compound **2** and compound **11** shows favorable receptor-ligand interactions, the positive binding energies indicate that these complexes may not be as stable as those with negative binding energies.

Table 5 MM-PBSA calculation for compounds **2**, **11**, **20**, and A26 after molecular dynamics simulations in the active site of *pf*DHODH.

Energy	Energy value (kJ/mol)			
	2	**11**	**20**	**A26**
EpotRecept+	−43.30 ± 80.52	−99.25 ± 21.07	−45.56 ± 19.13	−34.56 ± 20.43
EsolvRecept+	−16.86 ± 0.59	−67.21 ± 9.52	−14.76 ± 3.01	−3.76 ± 4.31

Energy	Energy value (kJ/mol)			
	2	**11**	**20**	**A26**
EpotLigand+	−13,305.47 ± 15,546.76	−14,145.26 ± 794.70	−14,493.54 ± 702.73	−14,482.54 ± 704.03
EsolvLigand−	−33,129.16 ± 586.56	−31,980.18 ± 1,413.19	−31,507.51 ± 1,217.81	−31,496.51 ± 1,219.11
EpotComplex−	−13,566.65 ± 15,660.02	−14,474.94 ± 791.81	−14,748.12 ± 706.55	−14,737.12 ± 707.85
EsolvComplex	−33,030.32 ± 633.16	−31,927.31 ± 1,411.70	−31,458.91 ± 1,226.51	−31,447.91 ± 1,227.81
Binding energy	102.22 ± 79.92	110.46 ± 29.60	145.70 ± 27.47	156.70 ± 28.77

The pharmacokinetic parameters of compounds **2**, **3**, **5**, and **11** (**Table 6**) provide comprehensive insights into their drug-like properties and potential as therapeutic agents. In terms of drug-likeness, all compounds have similar molecular weights, with compound **11** being slightly heavier at 358.39 g/mol. The log P values, which indicate lipophilicity, are also comparable, ranging from 3.76 to 4.16, suggesting moderate lipophilicity. The number of hydrogen bond donors and acceptors varies slightly, with compounds **11** having an additional acceptor. The topological polar surface area (TPSA) is higher for compounds **11** and **12**, which could affect their permeability and solubility. According to that criterias, none of the compounds show any violations of drug-likeness properties.

Regarding absorption, compounds **11** exhibits better water solubility compared to compounds **2**, **3**, and **5**, which may enhance their bioavailability. The human intestinal absorption (HIA) is high for all compounds, indicating good absorption potential. Caco-2 permeability values suggest moderate permeability across cell membranes. In terms of distribution, the log BBB permeability values indicate that compound **11** may has slightly better brain penetration, although all compounds show limited CNS permeability.

Table 6 ADMET results of quinazolinones.

Pharmacokinetic parameter	2	3	5	11
Drug-likeness				
Molecular weight (g/mol)	298.34	314.34	314.34	358.39
Log P	4.05	3.76	3.76	4.16
H-bond donor	0	1	1	1
H-bond acceptor	3	3	3	4
Topological polar surface area (Å^2)	34.89	55.12	55.12	64.35
Rotatable bonds	2	2	2	4
Absorption				
Water solubility (log mol/L)	−7.22	−5.42	−5.39	−3.33
HIA (%)	100	99.15	99.45	99.36
Caco-2 permeability (cm/s)	1.66	1.24	1.27	1.13
Distribution				
log BBB permeability	0.29	−0.02	−0.05	−0.15
VDss for human	−0.33	−1	−0.65	−1.05

Pharmacokinetic parameter	2	3	5	11
CNS permeability	−1.10	−1.83	−1.84	−2.14
Metabolism				
CYP2D6 inhibitor	Inactive	Inactive	Inactive	Inactive
CYP2E1 inhibitor	Inactive	Inactive	Inactive	Inactive
CYP3A4 inhibitor	Inactive	Inactive	Inactive	Inactive
CYP2C9 inhibitor	Inactive	Inactive	Inactive	Inactive
CYP2C19 inhibitor	Inactive	Inactive	Inactive	Inactive
CYP1A2 inhibitor	Inactive	Inactive	Inactive	Inactive
Excretion				
Total clearance (log mL/min/kg)	0.69	0.53	0.59	0.66
Renal OCT2 substrate	No	No	No	No
Toxicity				
Cytotoxicity	Inactive	Inactive	Inactive	Inactive
Mutagenicity	Inactive	Inactive	Inactive	Inactive
Cardiotoxicity	Inactive	Inactive	Inactive	Inactive
hERG I inhibitor	Inactive	Inactive	Inactive	Inactive
hERG II inhibitor	Active	Active	Active	Active
LD_{50} (mol/kg)	1.78	2.59	2.40	2.36

The metabolism data for compounds **2**, **3**, **5**, and **11** show that all these compounds are inactive as inhibitors for the major cytochrome P450 enzymes, including CYP2D6, CYP2E1, CYP3A4, CYP2C9, CYP2C19, and CYP1A2. This indicates that none of these compounds inhibit the key enzymes responsible for drug metabolism, which suggests a lower likelihood of drug-drug interactions caused by enzyme inhibition. Such inactivity against major CYP enzymes is favorable for drug candidates, as it reduces the risk of adverse metabolic interactions when co-administered with other medications.

For excretion, the total clearance rates are moderate, and none of the compounds are substrates for the renal OCT2 transporter. Toxicity assessments reveal that all compounds are inactive in terms of cytotoxicity, mutagenicity, and cardiotoxicity, although they are active as hERG II inhibitors, which could be a concern for cardiac safety. The LD_{50} values suggest moderate toxicity, with compound **3** having the highest tolerance at 2.59 mol/kg. Overall, these pharmacokinetic profiles suggest that compounds **2**, **3**, **5**, and **11** have potential as therapeutic agents but require further optimization to address potential safety concerns.

Conclusions and recommendations

This study focuses on the development of quinazolinone derivatives as potential inhibitors of *pf*DHFR and *pf*DHODH, enzymes essential for the survival of *Plasmodium falciparum*. To evaluate the efficacy and pharmacokinetic properties of these compounds, molecular docking, molecular dynamics simulations, MM-PBSA, and ADMET analyses were conducted.

Docking results revealed that compounds **3**, **5**, and **12** show stronger binding affinities to the *pf*DHFR protein than the native ligand WR99210, with binding energy values of −8.62, −8.46, −8.49, and −5.59 kcal/mol, respectively. These compounds form key hydrogen bonds and hydrophobic interactions with critical active site residues, which are vital for their inhibitory activity. In a similar manner, compounds **2**,

11, and **20** demonstrated higher binding affinities to the *pf*DHODH protein compared to the native ligand A26, with binding energies of −9.59, −10.12, −9.96, and −5.06 kcal/mol, respectively. All these compounds also engage in hydrogen bonding with the same crucial amino acid residues as the native ligand.

Molecular dynamics simulations further confirmed that compounds **3** and **5** maintained stability when bound to the *pf*DHFR protein, while compounds **2**, **11**, and **20** remained stable with the *pf*DHODH protein throughout a 100 ns simulation. MM-PBSA analysis showed that compounds **3** and **5** had negative binding energy values, although less favorable than the native ligand WR99210 for *pf*DHFR. Conversely, compounds **2**, **11**, and **20** exhibited better binding energies than the native ligand A26 for *pf*DHODH, despite all showing positive binding energy values. Additionally, compounds **2**, **3**, **5**, and **11** displayed favorable drug-likeness properties and acceptable ADMET profiles without significant violations. Among all the analyses conducted, compound 5 emerged as the most promising candidate.

Based on these findings, future research should focus on optimizing the synthesis methods and reaction conditions for quinazolinone derivatives. Expanding both *in vitro* and *in vivo* studies is essential to evaluate their effectiveness against drug-resistant *Plasmodium falciparum* strains, as well as their pharmacokinetic and toxicity characteristics. Furthermore, exploring potential synergistic effects with existing antimalarial drugs could lead to promising combination therapies, thus enhancing treatment efficacy.

Acknowledgements

This research is supported by the Ministry of Education, Culture, Research, and Technology and the Education Fund Management Institute through the PRPB Funding, PHC-Nusantara Program with contract number of 4920/UN1/DITLIT/PT.01.03/2024.

Declaration of generative AI in scientific writing

All the scientific content, analysis, interpretation and conclusions presented in the paper were independently developed by the authors.

CRediT author statement

Tendy Oktriawan: Data curation, Formal analysis, Investigation, Methodology, Writing – original draft, and Writing – review & editing. **Bina Agustin Aulia**: Formal analysis, Writing – review & editing. **Timur Setyawan**: Formal analysis, Writing – review & editing. **Muhammad Idham Darussalam Mardjan, Laurent Commeiras, Winarto Haryadi**: Conceptualization, Supervision, Funding acquisition, Project administration, Methodology, Validation, and Writing – review & editing. **Tri Joko Raharjo**: Software, Validation, and Writing – review & editing.

References

[1] A Alemu, B Lemma, T Bekele, G Geshere, EA Simma, CT Deressa and T Ketema. Malaria burden and associated risk factors among malaria suspected patients attending health facilities in Kaffa zone, Southwest Ethiopia. *Malaria Journal* 2024; **23(1)**, 397.

[2] J Li, HJ Docile, D Fisher, K Pronyuk and L Zhao. Current status of malaria control and elimination in Africa: Epidemiology, diagnosis, treatment, progress and challenges. *Journal of Epidemiology and Global Health* 2024; **14**, 561-579.

[3] W Haileselassie, R Adam, M Habtemichael, RE David, N Solomon, S Workineh, J Haider, A Belachew, W Deressa, G Yan, N Kassaw and D Parker. Socio-demographic and economic inequity in the use of insecticide-treated bed nets during pregnancy: A survey-based case study of 4 sub-Saharan African countries with a high burden of malaria. *Archives of Public Health* 2023; **81(1)**, 64.

[4] Y Wang, N Chitnis and E Fairbanks. Optimizing malaria vector control: A systematic review and mathematical modelling study to identify desirable characteristics of novel tools in different settings. *Parasites & Vectors* 2023. https://doi.org/10.21203/rs.3.rs-3332552/v1

[5] LP Hastuti, F Hermawan, MR Iresha and T Ernawati. *In-silico* studies of hydroxyxanthone derivatives as potential pfDHFR and pfDHODH inhibitor by molecular docking, molecular dynamics simulation, MM-PBSA calculation and pharmacokinetics prediction. *Informatics in Medicine Unlocked* 2024; **47**, 101485.

[6] S Johannsen, RM Gierse, A Krüger, RL Edwards, V Nanna, A Fontana, D Zhu, T Masini, E de Souza, M Droge, B van Vliet, J den Hartog, M Hutter, J Held, Odom, A John, C Wrenger and A Hirsch. High target homology does not guarantee inhibition: Aminothiazoles emerge as inhibitors of *Plasmodium falciparum*. *ACS Infectious Diseases* 2024; **10(3)**, 1000-1022.

[7] OB Akide Ndunge, N Kilian and MM Salman. Cerebral malaria and neuronal implications of *Plasmodium Falciparum* infection: From mechanisms to advanced models. *Advanced Science* 2022; **9(36)**, 202202944.

[8] TM Schäfer, L Pessanha de Carvalho, J Inoue, A Kreidenweiss and J Held. The problem of antimalarial resistance and its implications for drug discovery. *Expert Opinion on Drug Discovery* 2024; **19(2)**, 209-224.

[9] A Amusan, O Akinola, K Akano, M Hernández-Castañeda, JK Dick, A Sowunmi, G Hart and G Gbotosho. Frequency of chloroquine-resistant haplotype of Plasmodium falciparum (CVIET) in Ibadan, Southwest Nigeria 17 years post-chloroquine withdrawal. *Acta Tropica* 2024; **260**, 107435.

[10] G Matambisso, N Brokhattingen, S Maculuve, P Cístero, H Mbeve, A Escoda, G Bambo, B Cuna, C Melembe, N Ndimande, K Tetteh, C Drakeley, B Gamain, C Chitnis, V Chauhan, L Quinto, E Macete and A Mayor. Sustained clinical benefit of malaria chemoprevention with sulfadoxine-pyrimethamine (SP) in pregnant women in a region with high SP resistance markers. *Journal of Infection* 2024; **88**, 106144.

[11] E Kokori, G Olatunji, A Akinboade, A Akinoso, E Egbunu, SA Aremu, CE Okafor, O Oluwole and N Aderinto. Triple artemisinin-based combination therapy (TACT): advancing malaria control and eradication efforts. *Malaria Journal* 2024; **23**, 25.

[12] P Bravo, L Bizzarri, D Steinbrunn, J Lohse, AKH Hirsch, P Maser, M Rottmann and H Hahne. Integral solvent-induced protein precipitation for target-engagement studies in *Plasmodium falciparum*. *ACS Infectious Diseases* 2024; **10(12)**, 4073-4086.

[13] M Sharma, V Pandey, G Poli, T Tuccinardi, ML Lolli and VK Vyas. A Comprehensive review of synthetic strategies and sar studies for the discovery of *pf*DHODH inhibitors as antimalarial agents. Part 1: Triazolopyrimidine, Isoxazolopyrimidine and pyrrole-based (DSM) compounds. *Bioorganic Chemistry* 2024; **146**, 107249.

[14] PM Cheuka, P Njaria, G Mayoka and E Funjika. Emerging drug targets for antimalarial drug discovery: Validation and insights into molecular mechanisms of function. *Journal of Medicinal Chemistry* 2024; **67(2)**, 838-863.

[15] N Suwanakitti, Y Talawanich, J Vanichtanankul, S Taweechai, Y Yuthavong, S Kamchonwongpaisan and D Kongkasuriyachai. folA thyA knockout E. coli as a suitable surrogate model for evaluation of antifolate sensitivity against PfDHFR-TS. *Acta Tropica* 2024; **258**, 107360.

[16] H Shamshad, R Bakri and AZ Mirza. Dihydrofolate reductase, thymidylate synthase, and serine hydroxy methyltransferase: Successful targets against some infectious diseases. *Molecular Biology Reports* 2022; **49**, 6659-6691.

[17] X Zhang, Q Yang, X Zeng, Y Fu, Q Ding and Y Peng. Highly selective synthesis of selenium-containing (E)-N-propenolquinazolinones via FeCl 3-mediated cascade reaction of propargyl quinazoline-4-yl ethers with diselenides. *Organic & Biomolecular Chemistry* 2024; **22(47)**, 9231-9341.

[18] SS Acharya, S Patra, LM Barad, A Roul and BB Parida. Recent advances in iodine-DMSO mediated C(sp^3)-H functionalization of methyl-azaarenes *via* Kornblum oxidation. *New Journal of Chemistry* 2024; **48(17)**, 7614-7638.

[19] D Sengupta, D Sharma, RK Das, P Das, M Halder, P Rai and O Chakrabarti. Pioneering the photoactive relevance of quinazolinone-fullereropyrrolidine nanohybrids to address chemotherapeutic resistance in cancer. *ACS Medicinal Chemistry Letters* 2024; **15(7)**, 1118-1126.

[20] B Laleu, Y Akao, A Ochida, S Duffy, L Lucantoni, DM Shackleford, G Chen, K Katneni, F Chiu, K White, X Chen, A Sturm, K Dechering, B Crespo, L Sanz, B Wang, S Wittlin, S Charman, V Avery, N Cho and M Kamaura. Discovery and structure-

activity relationships of quinazolinone-2-carboxamide derivatives as novel orally efficacious antimalarials. *Journal of Medicinal Chemistry* 2021; **64(17)**, 12582-12602.

[21] UV Mhetre, NB Haval, GM Bondle, SS Rathod, PB Choudhari, J Kumari, D Sriram and KP Haval. Design, synthesis and molecular docking study of novel triazole-quinazolinone hybrids as antimalarial and antitubercular agents. *Bioorganic & Medicinal Chemistry Letters* 2024; **108**, 129800.

[22] JL Siqueira-Neto, KJ Wich, K Chibale, JN Burrows, DA Fidock and EA Winzeler. Author correction: Antimalarial drug discovery: Progress and approaches. *Nature Reviews Drug Discovery* 2024; **23**, 880.

[23] D Gheidari, M Mehrdad and Z Karimelahi. Virtual screening, ADMET prediction, molecular docking, and dynamic simulation studies of natural products as BACE1 inhibitors for the management of Alzheimer's disease. *Scientific Reports* 2024; **14(1)**, 26431.

[24] X Huang and J Hu. *In silico* discovery of novel androgen receptor inhibitors for prostate cancer therapy using virtual screening, molecular docking, and molecular dynamics simulations. *Scientific Reports* 2025; **15**, 29404.

[25] A Trezza, A Visibelli, B Roncaglia, R Barletta, S Iannielli, L Mahboob, O Spiga and A Santucci. Unveiling dynamic hotspots in protein-ligand binding: Accelerating target and drug discovery approaches. *International Journal of Molecular Sciences* 2025; **26(9)**, 3971.

[26] S Ghani, N Khan, H Sable, F Yao and M Shafiq. *Computational techniques for enhancing PK/PD modeling and simulation and ADMET prediction*. *In*: M Ishfaq (Ed.). Computational methods in medicinal chemistry, pharmacology, and toxicology. Academic Press, New York, 2025, p. 153-174.

[27] AB Reddy, TR Allaka, VSR Avuthu, K Chepuri, MZ Ahmed and H Nagarajaiah. New quinazolinone-1,2,4-triazole analogues: Synthesis, anticancer evaluation, molecular docking, and *in silico* ADMET prediction. *Journal of Molecular Structure* 2025; **1334**, 141850.

[28] MA Alamri, O Afzal, MJ Akhtar, S Karim, M Husain, MA Alossaimi and Y Riadi. Synthesis, *in silico* and *in vitro* studies of novel quinazolinone derivatives as potential SARS-CoV-2 3CLpro inhibitors. *Arabian Journal of Chemistry* 2024; **17(1)**, 105384.

[29] AA Alsfouk, IMM Othman, MM Anwar, A Saleh, NY Tashkandi and ES Nossier. New quinazolinone-based heterocyclic compounds as promising antimicrobial agents: Development, DNA gyrase B/topoisomerase IV inhibition activity, and *in silico* computational studies. *Journal of Molecular Structure* 2025; **1344**, 142953.

[30] YS Kurniawan, E Yudha, G Nugraha, N Fatmasari, HD Pranowo, J Jumina and EN Sholikhah. Molecular docking and molecular dynamic investigations of xanthone-chalcone derivatives against epidermal growth factor receptor for preliminary discovery of novel anticancer agent. *Indonesian Journal of Chemistry* 2024; **24(1)**, 250-266.

[31] MO Miranda, DJR Duarte and VM Rayón. The influence of halogen-mediated interactions on halogen abstraction reactions by formyl radicals. *Physical Chemistry Chemical Physics* 2025; **27(6)**, 3330-3340.

[32] PR Varadwaj, HM Marques and A Varadwaj. π-hole halogen bonds are sister interactions to σ-hole halogen bonds. *Crystal Growth & Design* 2024; **24(19)**, 7789-7807.

[33] R Canabal and C González-Bello. Chemical sensors for the early diagnosis of bacterial resistance to β-lactam antibiotics. *Bioorganic Chemistry* 2024; **150**, 107528.

[34] RA Laskowski, J Jabłońska, L Pravda, RS Vařeková and JM Thornton. PDBsum: Structural summaries of PDB entries. *Protein Science* 2018; **27(1)**, 129-134.

[35] K Saritha, M Alivelu and M Mohammad. Drug-likeness analysis, *in silico* ADMET profiling of compounds in Kedrostis foetidissima (Jacq.) Cogn, and antibacterial activity of the plant extract. *In Silico Pharmacology* 2024; **12(2)**, 67.

[36] MY Alsedfy, AA Ebnalwaled, M Moustafa and AH Said. Investigating the binding affinity, molecular dynamics, and ADMET properties of

curcumin-IONPs as a mucoadhesive bioavailable oral treatment for iron deficiency anemia. *Scientific Reports* 2024; **14**, 22027.

[37] H Guterres and W Im. CHARMM-GUI-based induced fit docking workflow to generate reliable protein-ligand binding modes. *Journal of Chemical Information and Modeling* 2023; **63(15)**, 4772-4779.

[38] R Touir, N Errahmany, M Rbaa, F Benhiba, M Doubi, EH EL Kafssaoui and B Lakhrissi. Experimental and computational chemistry investigation of the molecular structures of new synthetic quinazolinone derivatives as acid corrosion inhibitors for mild steel. *Journal of Molecular Structure* 2024; **1303**, 137499.

[39] GO Oduselu, OF Elebiju, TA Ogunnupebi, S Akash, OO Ajani and E Adebiyi. Employing hexahydroquinolines as PfCDPK4 inhibitors to combat malaria transmission: An advanced computational approach. *Advances and Applications in Bioinformatics and Chemistry* 2024; **17**, 83-105.

[40] MA Ojong, N Mujafarkani, FAK Khazaal, AS Hussam, OC Godfrey, K Muzammil, A Ahamed, R Edadi, I Anyambula, E Moses and I Benjamin. Investigating the impact of solvation on p-Phenylenediamine-2-Amino pyrimidine-Formaldehyde Terpolymer (P2APF) ligand's reactivity and drug suitability for malaria treatment: Insights from experimental and quantum calculations. *Journal of Molecular Structure* 2024; **1310**, 138113.

[41] S Jaiswal, K Verma, A Srivastva, N Arya, J Dwivedi and S Sharma. Green synthetic and pharmacological developments in the hybrid quinazolinone moiety: An updated review. *Current Topics in Medicinal Chemistry* 2025; **25(5)**, 493-532.

[42] MM Mansouri, L Emami, Z Rezaei and S Khabnadideh. Design, synthesis, biological assessments and computational studies of 3-substituted phenyl quinazolinone derivatives as promising anti-cancer agents. *BMC Chemistry* 2025; **19(1)**, 125.

[43] RM Hassan, H Yehia, MF El-Behairy, AAS El-Azzouny and MN Aboul-Enein. Design and synthesis of new quinazolinone derivatives: investigation of antimicrobial and biofilm inhibition effects. *Molecular Diversity* 2025; **29(1)**, 21-42.

[44] S Moghadam Farid, S Moradi Dehaghi, A Iraji, M Mahdavi and M Saeedi. Synthesis, biological evaluations, and *in silico* assessments of phenylamino quinazolinones as tyrosinase inhibitors. *Scientific Reports* 2025; **15(1)**, 846.

[45] M Alruwaili, HH Alhassan, H Almutary and M Tahir ul Qamar. Computational identification of aspartic protease inhibitors for antimalarial drug development against Plasmodium Vivax. *Scientific Reports* 2025; **15**, 14824.

[46] I Sama-ae, P Muengthongon, A Tohlaeh, W Rukhachan, P Kiattikul, F Samaeng, A Mitklin, P Kwankaew, M Kotepui and A Kepan. Penicillium-derived inhibitors of *Plasmodium falciparum* lactate dehydrogenase (PfLDH): A computational approach for novel antimalarial therapy development. *Scientifica* 2025; **2025(1)**, 8838031.